Tunable multidispersive bands of inductive origin in piezoelectric phononic plates

K. Mekrache, R. Sainidou, P. Rembert, N. Stefanou, Bruno Morvan

Journal of Applied Physics

Tunable multidispersive bands of inductive origin in piezoelectric phononic plates

K. Mekrache,[1] R. Sainidou,[1] P. Rembert,[1, a)] N. Stefanou,[2] and B. Morvan[1]
[1)] *Laboratoire Ondes et Milieux Complexes UMR CNRS 6294, UNIHAVRE, Normandie University, 75 rue Bellot, 76600 Le Havre, France*
[2)] *Section of Condensed Matter Physics, National and Kapodistrian University of Athens, Panepistimioupolis, GR-157 84 Athens, Greece*

(Dated: 18 October 2021)

A variety of multidispersive, localized or extended in frequency, bands, induced by inductance-based external electric circuits in piezoelectric phononic plates, is studied both theoretically and experimentally in this work. Their origin, tightly related to an equivalent *LC*-circuit behavior is analyzed in detail and their interaction with the Lamb-like guided modes of the plate is also discussed. These bands, easily tuned by the choice of the parameters of the external electric circuitry lead to a non-destructive, real-time control of the dispersion characteristics of these structures. Our device and analysis can find application in improvement of surface acoustic wave (SAW) components, by offering additional degrees of freedom.

I. INTRODUCTION

Controlling the dispersion of elastic waves has become a key issue when dealing with sound mitigation, vibration energy harvesting and, more generally, applications in which elastic waves have to be guided, collimated or trapped. The use of metamaterials has been an important step towards the feasibility of this control[1–3] by shaping the dispersion relation of these complex media. Several approaches have been proposed, the most common being the periodic structuration of the medium (phononic crystal) leading to folding of its frequency bands and opening up of band gaps. To tailor the band structure at subwavelength regime, a very promising means has been the use of the locally-resonant materials that produce strong dispersive effects related to negative effective bulk modulus and mass density[4–6]. These structures suffer, however, from an intrinsic narrow frequency range behavior of the resonant phenomena. To overcome this limitation, a more sophisticated structuring has been recently proposed, facilitated by the use of new manufacturing techniques, such as 3D printing. The concepts of rainbow metamaterials, gradient index and hierarchical metamaterials allowing to model the dispersion of the waves on a broader frequency range have emerged[7–9].

However all these attractive properties of metamaterials, even in the case of wide-range frequency phenomena, will stay less appealing, especially for application purposes, if the question of frequency tunability in their response is not answered. For a fixed geometrical arrangement of the constituents of the complex medium, the resulting frequency response cannot be adapted in real time in a real device. A simple way to introduce this frequency tunability/agility lies in the use of active components whose control can be achieved with the help of an externally applied field (magnetic[10,11], electric[12], thermal[13,14], and radiative[15,16]). The mechanical properties (mass density, elastic moduli) of the active component are thus modified, leading to reversible changes in its frequency band structure. Among others, piezoelectric-based structures have been shown to be excellent candidates for the real-time control of the propagation of elastic waves. The electro-mechanical coupling, naturally present in these materials, offers a versatile tool to shape the effective elastic properties of the metamaterial, through a variety of electrically controlled external conditions applied at the structure[17–26].

In this paper, we use a piezoelectric material as a substrate (plate) on which metallic strips (electrodes) are structured. In previous works[23–26], some of us have shown that propagation of Lamb-like guided modes in these phononic crystal piezoceramic plates exhibits an interesting tunable character easily controlled by external electric circuits through appropriate electric boundary conditions (EBCs) applied at the metallic strips. In particular, the band structure of the plate is significantly modulated by the presence of electric resonant modes originating from the external inductance-loads coupled to the effective capacitive behavior of the piezoelectric plate. Some basic methodological tools of our analysis are already presented in Ref. 26. Here, we extend them in order to give a synthetic panel that these systems can offer. We review under a new light some of the possibilities to mould the dispersion characteristics of tunable localized bands originating from an equivalent *LC*-circuit behavior, inherent in piezoelectric phononic plates, when loaded with inductance external circuits. We focus on three typical representative cases including external *L*-based loads that generate, each of them, a variety of multidispersive, tunable bands of electromagnetic (EM) origin, easily controlled via the external circuitry parameters (the inductance, in our case). These cases, first given in a qualitative schematic manner, cover, respectively, low, intermediate and higher frequency regions in a typical dispersion plot. Moreover, compared to previ-

[a)] Electronic mail: pascal.rembert@univ-lehavre.fr

ous works[23–26], an important improvement of our experimental device —especially its electronic part— is made, towards a wider range of choices in real-time control and automatization, combined to a robust and promising signal processing technique leading to a finer analysis of the experimental data. Usually, surface acoustic wave (SAW) devices offer only input and output ports, restricting the analysis exclusively in the frequency domain. Our device, allows to probe the surface waves along their path, thus offering the wavevector projection along this path as an additional degrees of freedom, which could provide an improvement in the domain of SAW components.

The paper is organized as follows. In Sec. II we present the general characteristics of the materials and structures considered in this study, and provide all necessary details concerning the experimental setup employed for our measurements, as well as the methods and techniques used in the analysis of the experimental data and in the numerical calculations, that follow in Sec. III. For the different structures under study, the analysis of their dispersion properties, strongly influenced by the external loads, in terms of underlying physical mechanisms responsible for these effects, as well as in comparison with their experimental observation, constitute the main part of Sec. III, before concluding the paper in Sec. IV.

II. MATERIALS AND METHODS

A. Sample structure

We shall be concerned, in this study, with thin homogeneous piezoceramic plates whose both surfaces are decorated with periodic one-dimensional (1D) arrays (lattice constant a_0) of parallel and face-to-face metallic strips of width w and negligible thickness. A schematic representation of the structure is given in Fig. 1(a). The plate is made of PZT (Navy VI) and in all theoretical calculations presented in this paper it will be considered to be infinite along x_1- and x_2-directions that coincide with the transversely isotropic plane of the piezoceramic material; the x_3-axis coincides with the polarization axis of the material.

The sample used in the experiments, is a finite square-shaped plate (edge length 48 mm and thickness $h = 1.6$ mm), as can be seen in Fig. 1(b), on both sides of which silver strips (rectangular electrodes) have been deposited periodically; their thickness is of the order of 15 μm and will be neglected in what follows. In the real structure, the lattice period dictated by the metallic strips (width $w = 0.7$ mm, separation gap $s = 0.3$ mm) equals $a_0 = s + w = 1$ mm, but as we have already explained in previous works[24–26] the true lattice constant of the crystal a can be non-destructively extended to be a multiple of a_0, controlled through the application of appropriate EBCs at each pair of (up- and down-side) electrodes. The latter is connected in the most general case to external electric circuits of characteristic impedance Z^{u} and Z^{d}, as schematically depicted in Fig. 1(c). In this manner, the elementary blocks of length $a_0 = w + s$ may have identical ($a = a_0$) or different ($a = \kappa a_0$, $\kappa = 2, 3, \ldots$) EBCs throughout the structure, thus tuning at will the real periodicity of the crystal. The 1D Brillouin zone (BZ) of the crystal is accordingly shortened; we will denote its center ($k_1 a/\pi = 0$) by Γ and its edge ($k_1 a/\pi = 1$) by X.

B. Experimental setup

Our experimental setup, though simple, is designed in such a general manner to facilitate modification at will of the EBCs applied at each electrode by connecting external circuits (resistive, capacitive, and/or inductive). The current version has substantially improved, as compared to the one used in Ref. 26. First, the plate is inserted into a 1 mm-pitch PCI Express® edge card reader (stackable female connector with 98 contacts), allowing connection of the electrodes of the crystal to different electric impedances, through controlled switches (FST3125). All connections are now realized in a secure and robust manner avoiding any noise and parasitic effects arising from soldering. Second, a microcontroller (Teensy 3.6) is used to actuate these switches, thus making possible a real-time control. Apart from the first pair of electrodes reserved for the excitation of the plate, the remaining 47 pairs of electrodes will be used to load the plate with external circuits, as shown in Fig. 2(a). Only this part of the plate (we will refer to it as loaded crystal hereafter) will be utilized to image the frequency response of the structure, except otherwise stated.

A 200V-amplitude and 0.1μs-width pulse signal is applied to the first pair of electrodes at the one edge of the piezoelectric plate, using a Panametrics 5058PR pulse generator, to excite guided waves within the plate. The incident beam penetrates into the loaded crystal and is reflected back at the other edge. To visualize the frequency response of the crystal, we employ an all-electric experimental technique (more details can be found in Ref. 26). After excitation of the piezoelectric plate, any deformations producing not negligible thickness variations of the plate will be manifested as electric potential variations on the electrodes through the electromechanical coupling that takes place within the piezoelectric material; we exclusively measure these electric potentials along the plate. To this end, a second PCI card reader, identical to the first one used for the loading by external circuits, is connected to the remaining free edge of the plate [Fig. 2(b)]. The electric potential is recorded with a 10-bit quantification, at each electrode position, on the upper or lower side of the plate, with the help of a digital oscilloscope (LeCroy HRO66ZI WaveRunner), the ground of the pulse generator being taken as reference;

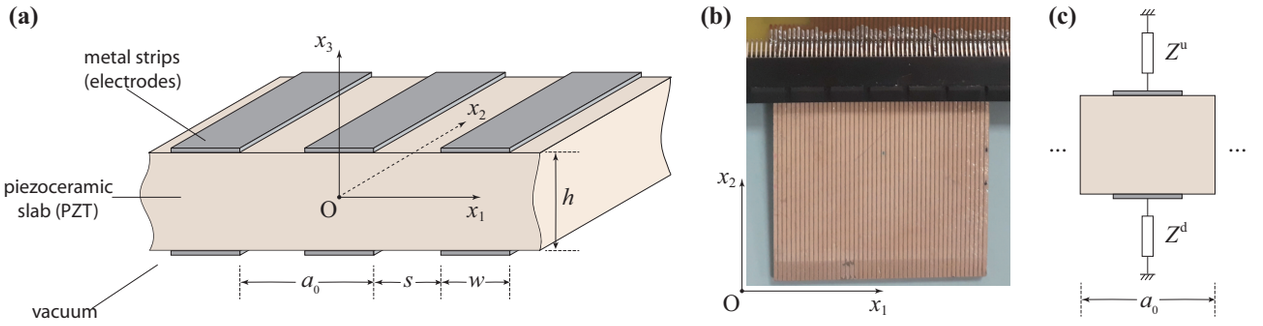

FIG. 1. (a) Schematic representation of the one-dimensional piezoelectric crystal, extended to infinity along x_1- and x_2-directions coinciding with the transversely isotropic plane of the piezoceramic material, poled across its thickness along the x_3 symmetry axis. (b) An image of the fabricated sample with finite dimensions (48 mm × 48 mm × 1.6 mm), used in the experiments; the metallic strips (width $w = 0.7$ mm and separation gap $s = 0.3$ mm) aligned along x_2-direction are connected at the top edge of the plate to a PCI reader. The structure consists of $N = 48$ elementary blocks of length $a_0 = 1$ mm. In (c) an elementary block of the structure loaded with electric circuits of impedance $Z^{\rm u}$ (upper plate side) and $Z^{\rm d}$ (lower plate side).

TABLE I. Material parameters for PZT (Navy VI), used in the calculations.

Material Property	Symbol	Value[a]
Elastic coefficients c^E_{pq} [GPa]	c^E_{11}	114.0
	c^E_{12}	75.7
	c^E_{13}	70.0 (72.4)
	c^E_{33}	107.0 (111.0)
	c^E_{44}	20.0 (26.3)
	$c^{E\,b}_{66}$	19.2
Piezoelectric coefficients e_{ip} [C m^{-2}]	e_{15}	14.2 (16.2)
	e_{31}	−2.92
	e_{33}	20.3 (23.4)
Relative permittivity coefficients ϵ^S_{pq}	ϵ^S_{11}	2120.
	ϵ^S_{33}	1980.
Mass density [kg m^{-3}]	ρ	7510.[c] (7780.)

[a] In the parenthesis, we give —if different— the initial values as provided by the manufacturer[28].
[b] $c^E_{66} = \frac{1}{2}(c^E_{11} - c^E_{12})$.
[c] Measured.

the time window chosen is typically set to 250 μs, with a sampling period equal to 5 ns, allowing to observe a few forward and backward traveling waves after reflections at the edges of the plate. Each measured signal is then averaged 30 times to improve the signal-to-noise ratio. The above settings ensure a sufficiently high Nyquist frequency and accurate resolution of the spectra obtained through fast Fourier transforms (FFT).

C. Simulations and signal processing

All band structure calculations shown in this paper were obtained by the use of a finite-element commercial package[27] (except otherwise stated). Assuming translational invariance along x_2-direction, the unit cell is reduced to a rectangle and the metallic strips to lines of zero thickness, able to host surface electric charges. The classical constitutive equations of piezoelectricity (stresses as functions of strains and electric field) apply at the surface of the rectangle. The boundary conditions are: (i) continuity of all fields between adjacent cells and periodic (Bloch) conditions at the left and right boundaries of the same cell, and (ii) at the upper and lower edges of the cell, free stress conditions, together with discontinuity of the normal component of the electric displacement field related to the surface charge density across the interface, assuming a uniform distribution of charge along the line representing the metallic strip. Under this last assumption, the whole electrode is seen as an electric node, where Ohm's relation involving external impedance loads can be applied. We recall that a full comparison between an ab-initio analytical model using the above assumptions and this FEM approach was given in Ref. 25, leading to practically identical (graphically indiscernible) results for the band diagrams of these systems. We note in passing that only the positive part of the BZ will be represented, since the dispersion diagrams are symmetric with respect to the vertical (frequency) axis, in all cases discussed here. The material parameters (elastic, piezoelectric and coupling constants) for PZT used in the simulations are shown in Table I and were determined by adjusting the dispersion relation of a floating-potential crystal to the corresponding experimental data. The experimental dispersion relation $\omega(k_1)$, $\omega = 2\pi f$ being the angular frequency, was obtained, after applying a 2D FFT of the potential signals $V(x_{1,n}, t)$ measured at each electrode position $x_{1,n}$, $n = 2, 3, \ldots, 48$, of the upper and lower side of the corresponding finite plate, following the procedure described in Ref. 26. The simulation results agree very well with the experimental data (tolerance better than 3.2%).

The floating-potential EBCs were used as a benchmark; we are, however, interested in more complex unit cells. For the systems under study, the dispersion plot

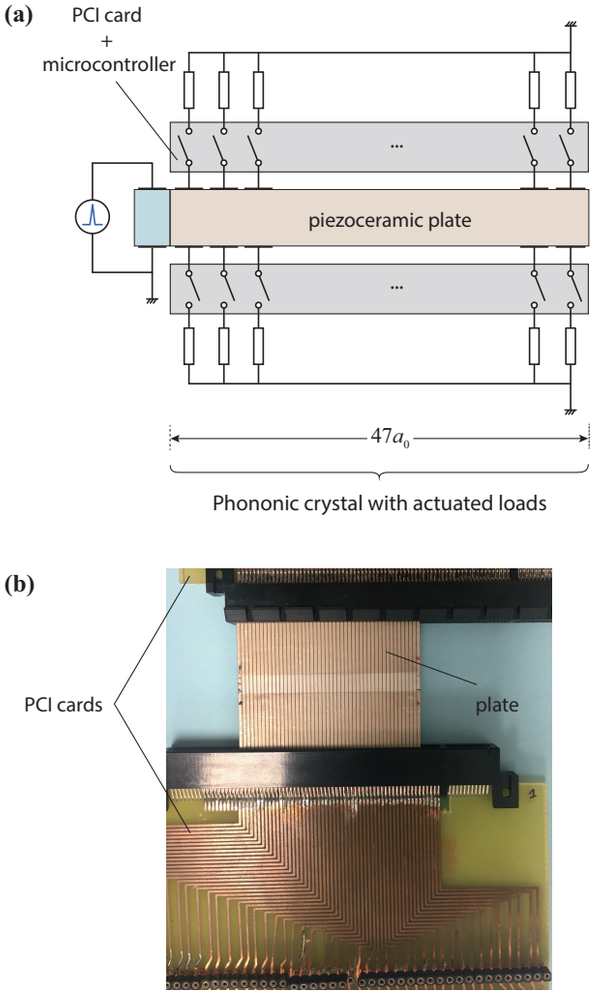

FIG. 2. The experimental setup used for the study of the phononic plate of Fig. 1: (a) schematic representation, and, (b) a view of the device. Excitation takes place at the left end of the plate and loading by external circuits at its remaining part through controlled EBCs.

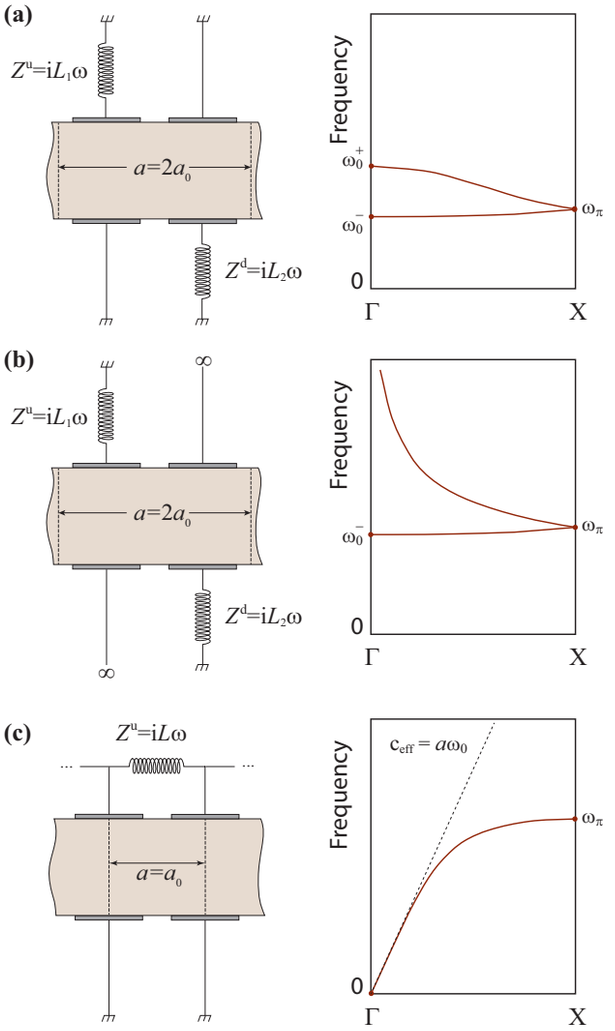

FIG. 3. The three configurations with inductive loads under study. Left panel: the unit cell of each crystal with different electric boundary conditions applied at the metallic strips [(a) grounded-inductance two-atom crystal, (b) floating-potential-inductance two-atom crystal, and (c) intercellular adjacent inductance-loaded crystal]. Right panel: schematic representation of the corresponding dispersion relation of the induced LC-origin bands (for $L_1 = L_2$, when applicable).

is more crowded: several eigenmode trajectories coexist in the ω-k_1 space at neighboring points and cannot be easily resolved, after a 2D FFT is performed. To better resolve these separate contributions, we opt for a different method of analysis, by adapting an autoregressive model to two dimensions (AR2D), i.e., to both space and time directions[29]. The results obtained in that manner agree with the corresponding picture obtained by a 2D FFT, without suffering from a wide ω-k_1 peak-character.

III. RESULTS AND DISCUSSION

In what follows, we will focus on three configurations, all of them using inductance loads on the unit cell of the crystal, shown schematically in the left panel of Fig. 3; their interest lies on the unusual multidispersive form of localized and/or extended frequency bands of inductive origin that this circuitry may offer. More precisely, the first two cases correspond to two-atom unit cells ($a = 2a_0$), constructed by combination of two antiparallel elementary blocks (of width a_0), each of them having a L-load on the one side of the plate, the other-side electrode being either shunted [Fig. 3(a)] or in floating potential [Fig. 3(b)]. Though inspired from Ref. 26, the resulting structures offer new possibilities, since they possess inversion symmetry and exhibit, respectively, a set of two flat bands of localized modes and a set of one flat and one infinitely extended hyperbola-like frequency

bands, as schematically depicted in the right panel of Fig. 3. A third configuration [see Fig. 3(c)] consists of a L-load connecting adjacent strips, the EBCs conserve, in that case, the spatial periodicity of the metallic array ($a = a_0$). The corresponding modes originating from this circuitry exhibit a linear dispersion behavior with an effective medium slope $c_{\text{eff}} = a\omega_0$ at the long-wavelength limit which bends and tends to a zero-group-velocity branch at X point. It is worth noting that such a configuration is a direct analogue of the unit cell of a transmission line governed by the well-known telegrapher's equation.

The different characteristic angular frequencies $\omega_0^{\pm}$, ω_0, ω_π, appearing in Fig. 3 to describe qualitatively the dispersion of these eigenmodes at Γ and X points of the BZ, depend of course of the choice of L and of some characteristic capacitance values C, C_s, C_1, and C_2 that describe effectively the intrinsic behavior of the piezoelectric plate in terms of equivalent circuits. More details are given in Appendix A. We note that this analysis for the two-atom crystals reveals higher-order interactions of capacitive origin within the plate which takes place between neighbors of adjacent cells and opposite sides, compared to previous demonstrations[26].

A. Grounded and inductance loaded two-atom unit cell

To begin with we shall examine the case of up- and down-side inductance loads alternated with grounded strips. The unit cell is thus a two-atom molecule analog with inversion symmetry if $L_1 = L_2$, or with identity operation symmetry only, if $L_1 \neq L_2$, as shown in Fig. 3(a). Aiming to analyze its frequency band structure both theoretically and experimentally, we find it useful to focus first on the frequency response of the corresponding monatomic crystal of lattice constant $a = a_0$ [suppose only the left half part of the unit cell of Fig. 3(a)]. In the absence of piezoelectric coupling ($e_{ij} = 0$), the eigenmodes of the crystal are separated into two independent, non-interacting subspaces: the elastic-displacement Lamb guided modes of the plate (labelled, hereafter, with A for antisymmetric and S for symmetric modes, following standard notation used for Lamb modes in plates), simply folded at the BZ edge ($k_1 a_0/\pi = 1$) and the EM modes which originate from an LC-equivalent circuit behavior of the unit cell. The electric resonances of these individual LC atoms interact between each other and form a cos-like resonant band. In Fig. 4(a) we show the calculated —using a finite-element method— frequency band structure of such a crystal, the first subspace shown in gray lines, the second one in blue dotted line, extending from 1.294 MHz ($k_1 = 0$) to 0.597 MHz ($k_1 = \pi/a_0$). We note in passing that this zero coupling analysis, already presented in previous works[24,26], can be employed to visualize the bands of EM origin before hybridization.

When two antiparallel atoms are brought together to form a two-atom unit cell as shown in Fig. 3(a) the BZ becomes shorter ($a = 2a_0$). An additional folding at $k_1 a_0/\pi = 0.5$ of the dispersion plot is dictated and, as a result, the EM resonant band is thus split into two separate flat minibands, a more dispersive, $\omega^+(k_1)$, extending from 0.839 MHz ($k_1 = 0$) to 0.732 MHz ($k_1 = \pi/a$), and a less dispersive, $\omega^-(k_1)$, extending from 0.708 MHz ($k_1 = 0$) to 0.732 MHz ($k_1 = \pi/a$). These bands compare very well (relative error better than ±0.9%) to a tight-binding description[30] with first-neighbour interactions between atomic sites [blue dashed lines in Fig. 4(a)] that leads to $\omega^{\pm}(k_1) = [\omega_{\text{at}}^2 + 2\gamma_1 \cos k_1 a \pm 2\gamma_2 \cos(k_1 a/2)]^{1/2}$, $\gamma_1 = \gamma(a)$, $\gamma_2 = \gamma(R)$ being the overlap integrals γ depending on the distance $a = 2a_0$ and $R = \sqrt{a_0^2 + h^2} = 1.89a_0$ between the centers of the atomic potential functions and ω_{at} the eigenfrequency of an isolated atom. By a best fitting procedure we find $\omega_{\text{at}}/(2\pi) = 0.753$ MHz, $\sqrt{\gamma_1}/(2\pi) = 0.128$ MHz, and $\sqrt{\gamma_2}/(2\pi) = 0.214$ MHz. The $\omega^{\pm}(k_1)$ bands are independently reproduced by the electric-circuit picture [see Eq. (A1) in Appendix A 1, with $C = 0.103$ nF, $C_s = 0.552$ nF, $C_1 = 0.0348$ nF, and

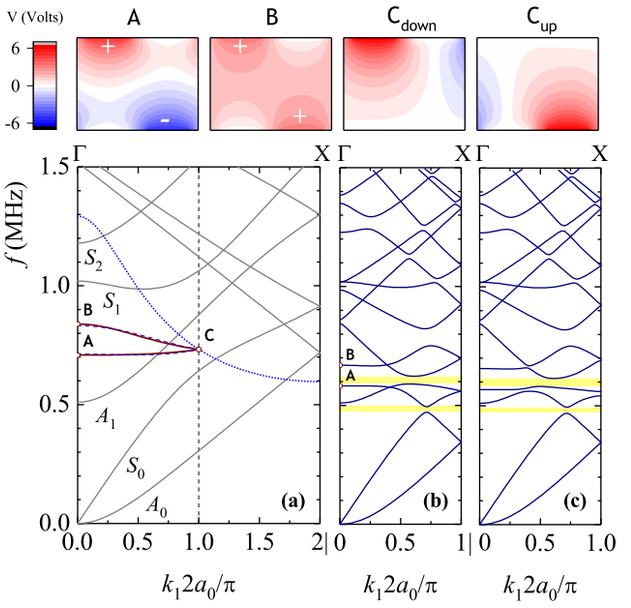

FIG. 4. (a) Calculated frequency band structure for a monoatomic crystal of lattice constant $a = a_0$ [only the left half part of the unit cell in Fig. 3(a) with $L_1 = 30$ μH is considered] when piezoelectric coupling is switched off. The blue dotted curve spanning the whole BZ indicates the EM resonance band, while the thick red line represents the same band for the diatomic crystal of lattice constant $a = 2a_0$ [unit cell of Fig. 3(a) with $L_1 = L_2 = 30$ μH]; the gray lines correspond to Lamb eigenmodes of the phononic plate, labelled following standard notation. The full calculation of the band structures for the diatomic crystal of Fig. 3(a) when piezoelectric coupling is taken into account is shown in (b) for $L_1 = L_2 = 30$ μH and (c) for $L_1 = 30$ μH and $L_2 = 33$ μH. Yellow-shaded regions denote absolute frequency gaps. Top panel: Potential field plots within a unit cell for the points labelled in (a).

$C_2 = 0.116$ nF obtained by a best fitting procedure], also in accordance with the above tight-binding model.

A more careful look at the potential field functions at Γ point plotted within the unit cell (see top panel of Fig. 4) reveals a bonding ($\Phi_+ = \mathcal{C}_+(\phi_1 + \phi_2)$) and antibonding ($\Phi_- = \mathcal{C}_-(\phi_1 - \phi_2)$) character in analogy with a diatomic molecule picture in quantum physics, ϕ_1 and ϕ_2 being the two atomic potential functions and $\mathcal{C}_\pm$ appropriate coefficients. Along ΓX direction the potential fields evolve progressively towards a more weighted one-atom picture with a double-degenerate state at X point (see two right plots of the top panel in Fig. 4), this degeneracy being lifted when inversion symmetry disappears ($L_1 \neq L_2$).

This picture is further modified when piezoelectric coupling is taken into account ($e_{ij} \neq 0$), as it should be in a real system. The result of our calculation is shown in Fig. 4(b). As a first remark, one observes a blue shift for the Lamb guided modes and a red shift for the EM origin resonant bands. And more importantly, the two eigenmode subspaces interact between each other and, in general, one expects the formation of avoided crossings between modes of the same symmetry. The lower in frequency EM resonant band $\omega^-(k_1)$ interacts with both the S_0 branch and the first folded A_0 branch, and similarly the higher in frequency EM band $\omega^+(k_1)$ interacts with both the A_1 branch and the first folded S_0 branch, thus leading to narrow selective absolute gaps (yellow-shaded regions). A slight detuning between L_1 and L_2 lowers further the symmetry of the system (inversion is now invalid) thus resulting in interactions, though very weak, between all bands [see Fig. 4(c)].

Next, we confirm the above predictions, by their experimental verification. We measured the potential signal $V(x_{1,n}, t)$ along the $n = 2, 3, \ldots, 48$ electrode positions located at the upper side of the plate, and after application of the AR2D model, we obtain the experimental $V(\omega, k_1)$, whose amplitude is shown in Fig. 5(a), and close to it, in Fig. 5(b), the calculated frequency band structure shown in Fig. 4(b). The different branches are color-indexed with the value of the potential, averaged on the area of the upper-side electrodes: the darker the trajectory, the weaker the electromechanical coupling, that takes place within the plate, is.

The experimental dispersion plot mainly reveals the S_0-like branches of positive slope in the positive part of the 1st and negative part of the 2nd BZ, that compare well to the corresponding theoretical curve with effective medium slope of 3013 m s^{-1} at the long wavelength limit. In addition, one observes some bright spots spanning the frequency region between 0.6 and 0.7 MHz, that could correspond to the localized modes of EM origin in Fig. 5(b) at about 0.58 MHz for $\omega^-(k_1)$ and at about 0.67 MHz for $\omega^+(k_1)$. At higher frequencies but below 1 MHz, two more trajectories are experimentally observed, belonging probably to A_1-like and S_0-like branches, visible in the positive part of the 1st and 2nd BZ, respectively (but also in the negative part of the 2nd and 1st BZ). The comparison between theory and experiment is, however, not straightforward, especially because the finite-element simulations predict much more active branches than seen experimentally.

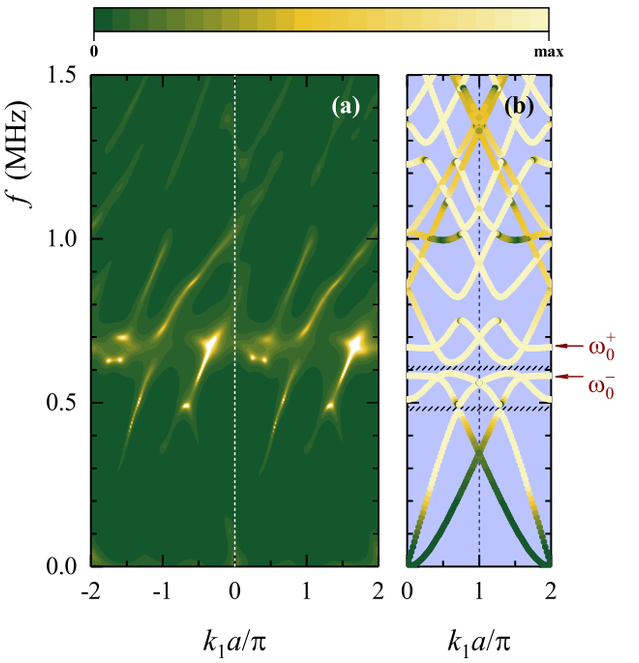

FIG. 5. Frequency band structure of the diatomic grounded-L piezoelectric phononic crystal (lattice constant $a = 2a_0 = 2$ mm) with EBCs depicted in Fig. 3(a). (a) Experimental dispersion plot for the finite crystal, consisting of $N = 24$ unit cells, obtained by use of the AR2D model on the electric-potential signal recorded at the upper-side electrode positions. (b) Calculated dispersion plot obtained through finite-element numerical simulations for the corresponding infinite crystal for $L = 30$ μH. In (a) the color map is saturated; in (b) the trajectories are color-indexed with the average potential on the upper-side electrodes of the unit cell. Red arrows and hatched areas denote, respectively, frequency bounds of the EM bands at Γ point and absolute gaps.

B. Floating potential and inductance loaded two-atom unit cell

If we replace the two grounded ends of the previous structure by free floating potential (FP) ends, we obtain the unit cell shown in Fig. 3(b). A similar methodology can be developed as that given in Sec. III A in order to follow the formation of the resonant bands; the main difference lies in the specific form of this band before hybridization. As it can be easily shown[31] this branch is hyperbolic for the corresponding monatomic crystal [consider only the left half part of the unit cell of Fig. 3(b)] and when constructing the diatomic unit cell, the folding results in two branches, one hyperbola-like, $\omega^+(k_1)$, extended in frequency, the other, $\omega^-(k_1)$, relatively flat. When $L_1 = L_2$ these two distinct bands degenerate to

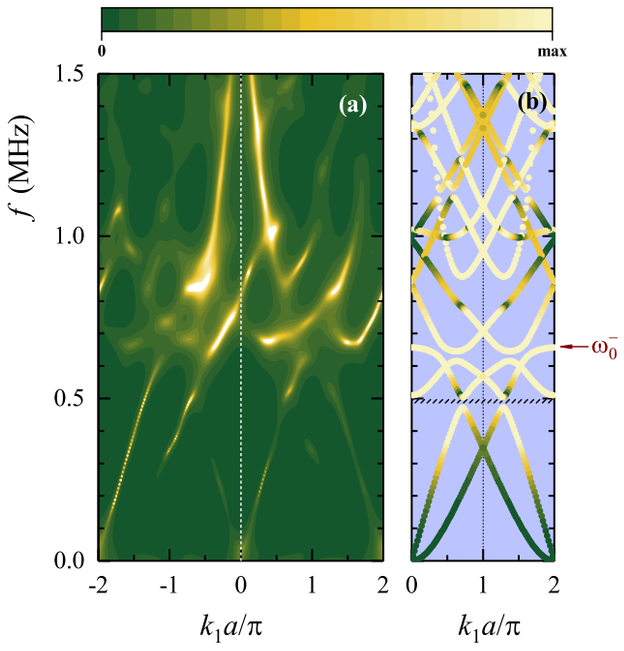

FIG. 6. Frequency band structure of the floating-potential-L piezoelectric phononic crystal (lattice constant $a = 2a_0 = 2$ mm) with EBCs depicted in Fig. 3(b). (a) Experimental dispersion plot for the finite crystal, consisting of $N = 24$ unit cells, obtained by use of the AR2D model on the electric-potential signal recorded at the upper-side electrode positions. (b) Calculated dispersion plot obtained through finite-element numerical simulations for the corresponding infinite crystal for $L = 30$ μH. In (a) the color map is saturated; in (b) the trajectories are color-indexed with the average potential on the upper-side electrodes of the unit cell. Red arrow and hatched area denote, respectively, frequency bounds of the EM band at Γ point and absolute gap.

a common frequency ω_π at X point; again this degeneracy originating from the inversion symmetry of the unit cell, is lifted if $L_1 \neq L_2$. The finite frequency point $\omega_0^- = \omega^-(k_1 = 0)$ can be tuned through the choice of L. Analytic expressions are derived in terms of an equivalent periodic transmission-line picture, as detailed in Appendix A 2.

The experimental frequency band structure of our finite-size sample is obtained following the same procedure, as for the previous case of grounded crystal (Sec. III A). The results are shown in Fig. 6(a), and next to it [Fig. 6(b)] the calculated frequency band structure for the corresponding infinite crystal, assuming again a pure L-component ($L = 30$ μH). In the experimental picture, three frequency regions are distinguished: below 0.6 MHz the S_0-like and A_0-like branches are clearly identified, in good agreement with those predicted theoretically, and this was also the case for the grounded crystal (Fig. 5). Next, for frequencies above 0.6 MHz and below 1.0 MHz some bright spots are observed but a one-to-one comparison to the theoretical picture becomes not straightforward. Finally, above 1.0 MHz the two extended, hyperbolic branches become dominant and are clearly observed within the 1st BZ, in both its positive and negative part.

In both cases examined up to now, we remark that the experimental dispersion plots [Figs. 5(a) and 6(a)] do not reveal all branches predicted theoretically, and, more importantly, symmetry operations such as translation symmetry by a reciprocal lattice vector, $\omega(k_1) = \omega(k_1 + \frac{2\pi}{a})$, and/or mirror symmetry, $\omega(k_1) = \omega(-k_1)$, are not observed for all trajectories. This could be explained by finite size effects and excitation that favors some of the branches with respect to others. To facilitate comparison to the theoretical picture, we artificially restore the above said lost symmetries, by taking the average on the positive-k_1 and negative-k_1 part after, i) horizontal flipping, and, ii) horizontal translation by 2 (in reduced k_1-axis units) of the latter. These two operations lead to a picture with mirror symmetry with respect to vertical (frequency) axis at both Γ and X points, thus the ΓX direction is sufficient for any analysis. The results are shown in Fig. 7, for the grounded crystal [left panel, plot (a)] and for the floating-potential crystal [right panel, plot (c)]. Their comparison to the corresponding theoretical predictions [Figs. 5(b) and 6(b)] reveals a red shift of the simulated EM modes. Obviously, the reality, far away from the numerous simplifications assumed in the simulations, includes finite size effects, different elastic boundary conditions at the edges of the plate due to the use of the PCI cards, and, real-electronics effects, present in the circuitry, that were neglected in the previous analysis. In fact, a Z_e impedance load (see Appendix B) will be considered instead of the idealized $Z^{\rm u} = Z^{\rm d} = Z_L = {\rm i}L\omega$ generated by a pure L-component. In plots (b) and (d) of Fig. 7 we show the calculated band structures that correspond to those of Figs. 5(b) and 6(b), but for the real load Z_e [Eq. (B1)] instead of the pure inductive load with $L = 30$ μH. The use of Z_e blue-shifts the EM modes [by about $\sim 10\%$ for $\omega_0^\pm$ with respect to those of Figs. 5(b) and 6(b), indicated here by red arrows as guides to the eye] and improves the comparison between experimental data and theoretical simulations. The EM modes manifest themselves as two flat bands lying in the frequency range from 0.6 to 0.75 MHz for the grounded-L crystal [Fig. 7(b)] in rather good agreement with the experimental picture [bright spots extending from 0.63 to 0.71 MHz in Fig. 7(a)]. For the floating-potential-L crystal [Fig. 7(d)] the EM modes manifest themselves, on the one hand, as a flat band centered at 0.7 MHz and, on the other hand, as a hyperbolic branch which interacts strongly with the A_1-like branch and spans the whole frequency range above 0.9 MHz; these compare well to the experimental picture [Fig. 7(c)] that reveals, respectively, a flat bright segment from 0.66 to 0.75 MHz and a hyperbolic branch above 0.82 MHz.

We note in passing the appearance of narrow, selective, absolute frequency gaps for both systems [see hatched areas in Figs. 7(b), (d)] originating from avoided-crossing

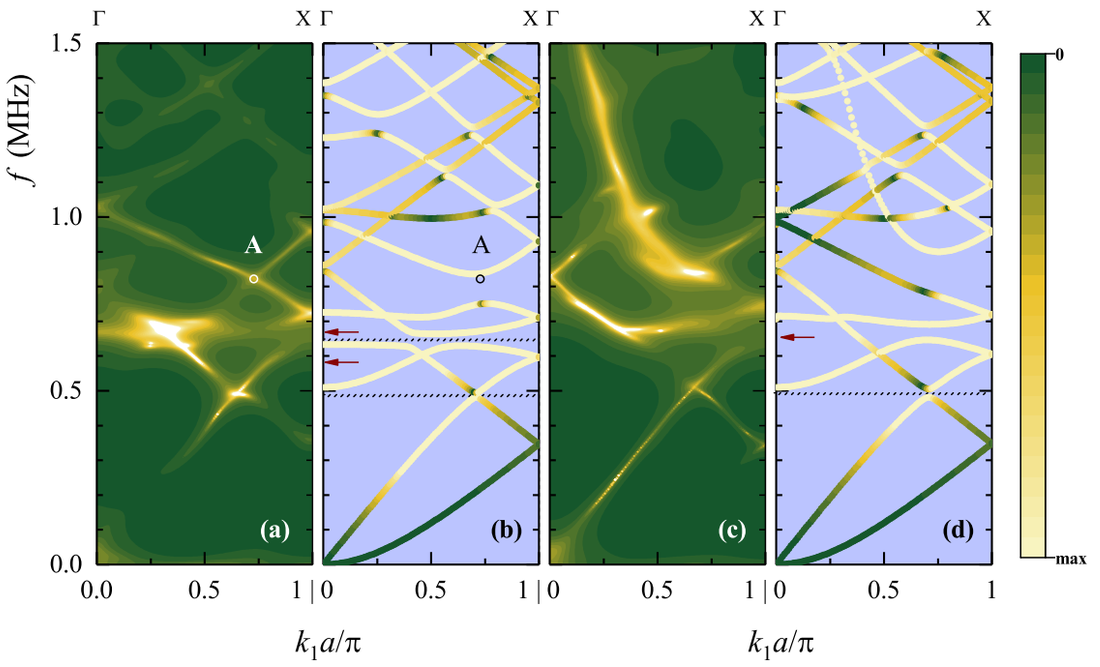

FIG. 7. Experimental frequency band structure of the diatomic (a) grounded-L and (c) floating-potential-L piezoelectric phononic crystals, after reduction along ΓX direction (see text) of their initial map plots, shown respectively in Figs. 5(a) and 6(a). In (b) and (d) the corresponding calculated dispersion plots for the infinite crystals, assuming real loads Z_e instead of the pure inductive ones $Z_{\rm L}$ ($L = 30$ μH). Red arrows denote the frequency positions of the EM bands at Γ point as predicted for the case of $Z_{\rm L}$ instead of Z_e [see Figs. 5(b) and 6(b), respectively]; hatched areas indicate, as usually, absolute gaps.

between bands of the same symmetry. Therefore, one expects that even structures with a small number of units will exhibit such type of gaps[32]. Their frequency position is indirectly controlled through ω_0 values scaling as $\sim L^{-1/2}$ [see Appendix A]. Their width is narrow, but possible enlargement could be achieved with electronic components facilitating the degree of interaction [e.g., negative capacitors[25]].

A careful global evaluation of the picture obtained by both models used for the simulations, i.e., Z_L and Z_e, for the two crystals under study, suggests that none of these can perfectly describe the experimental picture in terms of frequency position of the EM modes (they are in general slightly shifted, but the hyperbolic branch clearly blue-shifted in the simulations) and in terms of degree of interaction that takes place in the avoided-crossing regions when EM and Lamb-like modes cross each other [weak avoiding is experimentally observed, while a strong one is predicted, e.g. at point A in Figs. 7(a), (b)]. Deviations are also observed between some dark branch segments (vanishing potential value along them), while predicted highlighted in theory, e.g., the A_1-like branch which is theoretically predicted with a cut-off frequency close to 0.5 MHz is not experimentally discernible. We deduce that even if a pure L-component is too simple to reproduce exactly the experimental picture of the dispersion plot of these crystals, the use of the experimentally identified load Z_e is not sufficient either. A possible reason could be the modification of this individual-atom load Z_e (we recall that its identification has been realized under isolated conditions, outside the crystal) when it is introduced in our device including the plate itself and the system of two PCI cards. On the other hand, simulations still constitute idealized models, since they neglect any finite size effects and leakage of elastic and EM modes in the surrounding medium (air). For the above reasons, comparison between theory and experiments remains, however, very satisfactory and provides a good verification of the main features of the dispersion properties of these crystals.

C. Intercellular inductance loaded unit cell

As a last case, we examine a crystal plate with intercellular connection of adjacent strips located at the same side of the plate (say the upper one) via an inductance load L, the other-side strips being grounded, as depicted in Fig. 3(c). These EBCs conserve the periodicity of the metallic array. The numerically predicted band structure of that crystal (lattice constant $a = a_0$) is shown in Fig. 8 for two distinct inductance values: $L = 150$ μH [plot (a)] and $L = 30$ μH [plot (b)]. The most striking feature of these dispersion plots is the appearance of a linear-dispersion branch at the long-wavelength limit, in addition to the traditionally expected S_0-like and A_0-like

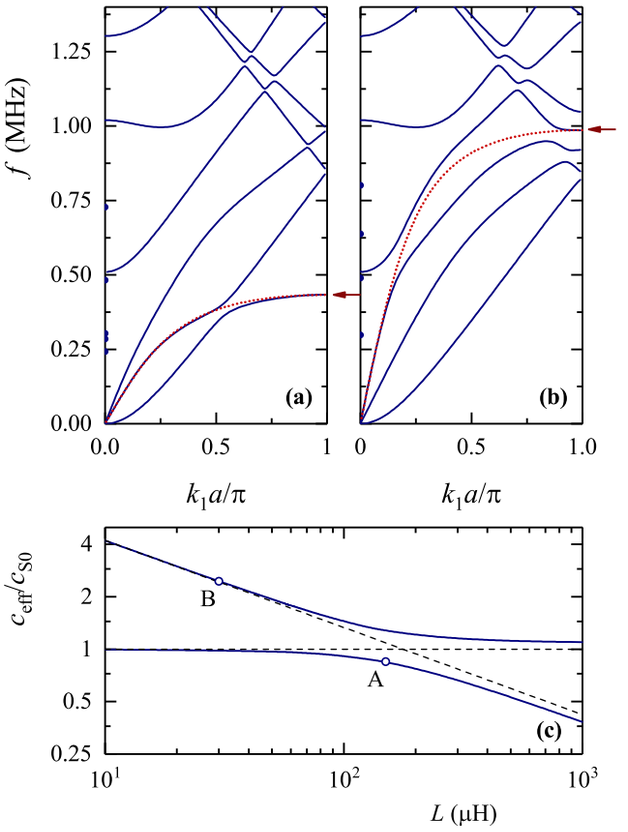

FIG. 8. Calculated frequency band structure for a monoatomic crystal of lattice constant $a = a_0$ whose unit cell is depicted in Fig. 3(c) with (a) $L = 150$ μH and (b) $L = 30$ μH. The dotted red lines represent an estimate of the unhybridized L-induced band, applying Eq. (A3) for appropriate values of the parameters C, C_s (see text), with starting parameters $\omega_\pi/(2\pi)$ (indicated by red arrows) and the long-wavelength slope, $c_{\rm eff}$, of this frequency branch. (c) Evolution of the slope of the two linear branches at $\omega \to 0$ for several values of the inductance load L. Horizontal and oblique dashed lines represent, respectively, the effective medium slope of the S_0 branch of the corresponding grounded crystal and the L-induced branch from Eq. (A3) calculated for C, C_s determined for $L = 10$ μH. Points A and B correspond to the L-induced bands (red dotted curves) of plots (a) and (b), respectively.

branches emerging at the same frequency range. The general form of that L-induced branch when the piezoelectric coupling is switched off ($e_{ij} = 0$) follows the schematic representation given in the right plot of Fig. 3(c) and is described by the relation (A3) for some appropriate values C, C_s in an equivalent periodic transmission line picture. The slope, $c_{\rm eff}$, of this L-branch is tuned via the choice of L, and covers a wide range of effective medium velocities not easily encountered in ordinary materials. The equivalent transmission line model presented in Appendix A predicts a scaling $\sim L^{-1/2}$ for given (L-independent) C and C_s values (we find $C = 0.645$ nF and $C_s = 0.593$ nF, for the crystal under study). When this coupling is switched on ($e_{ij} \neq 0$), as it should be in a real system, the L-induced band interacts with the same symmetry bands of Lamb eigenmodes and generates avoided-crossing effects. To facilitate its visualization before hybridization, we apply the same relation [Eq. (A3), with different values of C, C_s, reflecting all coupling effects] to model its unhybridized form, represented in Fig. 8(a) and (b) by red dotted lines: after a careful reading of these dispersion plots, we identify the two starting parameters, ω_π (indicated by a red arrow), and, $c_{\rm eff}$, the effective-medium slope of this branch at the long-wavelength limit, used to deduce the internal model capacitance parameters ($C = 0.737$ nF and $C_s = 0.868$ nF, for $L = 30$ μH; $C = 1.413$ nF and $C_s = 0.900$ nF, for $L = 150$ μH).

For the case of $L = 150$ μH [Fig. 8(a)], the L-band with $c_{\rm eff} = 2560$ m s^{-1} interacts weakly with the A_0-like branch, and a small avoided-crossing occurs at about 0.375 MHz; the other linear, S_0-like, branch has $c_{\rm eff} = 3850$ m s^{-1}, which is higher than the corresponding value in a grounded crystal, $c_{\rm S_0} = 3020$ m s^{-1}. For the case of $L = 30$ μH [Fig. 8(b)], the L-band with $c_{\rm eff} = 7400$ m s^{-1} interacts weakly with the A_1-like branch as well as with the first folded A_0-like branch, giving rise to relatively larger avoided crossings, occurring, respectively, at about 0.50 MHz and 0.95 MHz; the other linear, S_0-like, branch has $c_{\rm eff} = 2970$ m s^{-1}, which is lower than $c_{\rm S_0}$. The above suggest a possible interaction with the S_0-like branch when the two modes are close enough. In Fig. 8(c) we plot the evolution of the slope at the long-wavelength limit, for several values of the inductance covering a large range spanning over two orders of magnitude, of both linear branches of a typical dispersion plot as those shown in Fig. 8(a) and (b). One clearly observes a hybridization between two distinct modes: the S_0-like mode, represented by the horizontal dashed line, and the L-induced mode, represented by the oblique dashed line that corresponds to the $\sim L^{-1/2}$ scaling rule calculated at $L = 10$ μH (for $C/[1 + C/(4C_s)] = 0.618$ nF), far away from the crossing point that occurs in the vicinity of $L = 150$ μH. For this value of L, a high-degree hybridization takes place, both linear-dispersion modes carry both the S_0 and L-induced character, the point A corresponding to the L-induced band. On the contrary, for $L = 30$ μH point B, that corresponds to the L-induced band, conserves mainly its L-induced character.

We turn now our attention to the comparison with experimental results. As previously, the Z_e load will be considered instead of the idealized Z_L in the calculations. We measured the potential signal along the $n = 2, 3, \ldots, 48$ electrode positions located at the upper side of the plate, and after application of the AR2D model, we obtain the experimental $V(\omega, k_1)$ whose amplitude is shown in Fig. 9(a) that compares well with the calculated frequency band structure including the real load Z_e, in Fig. 9(b).

The linear-slope, effective-medium branch of EM origin, clearly observed in the experiments, is perfectly re-

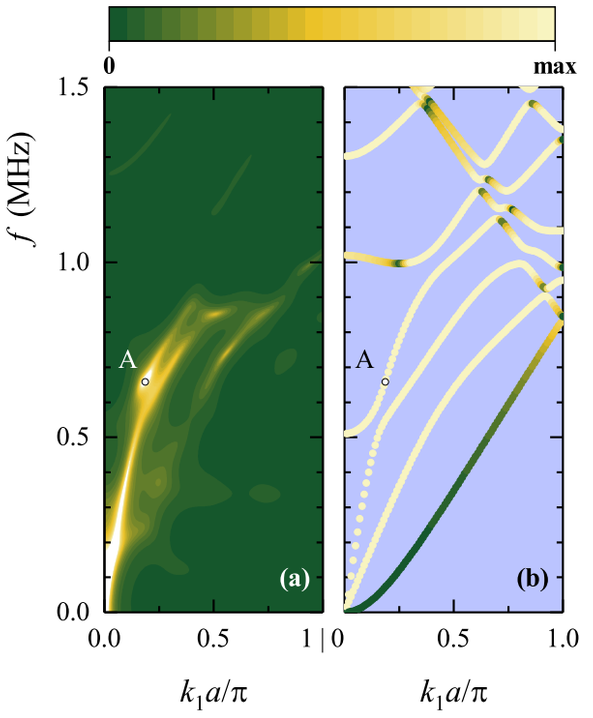

FIG. 9. (a) Experimental and (b) calculated frequency band structure for the monoatomic crystal of lattice constant $a = a_0$ whose unit cell is depicted in Fig. 3(c), loaded with impedance Z_e [Eq. (B1)]. In (b) the dispersion lines are color-indexed with the projection of the potential value averaged in the upper-side electrode of the unit cell.

produced in the calculations. The same holds for the bright part of the A_1-like branch [see point A in Fig. 9(a)], though the latter is not discernible experimentally close to its cut-off frequency at $\sim$ 0.5 MHz (this was also the case for the crystals presented in Sec. III A and III B). The S_0-like branch is also observed experimentally, though with lower amplitude than predicted in the theoretical calculation. We note that the latter fails to capture the degree of repulsion of the trajectories in the vicinity of point A and for frequencies above it (this avoiding is predicted to be larger than experimentally observed). We close this part by a general remark concerning the A_0-like branch which is not observed (apart some slightly visible parts close to X point), since the potential takes very low values along it, in all cases studied here, in perfect agreement with our numerical calculations.

IV. CONCLUSIONS

In conclusion, we have presented a thorough analysis of the dispersion properties of piezoelectric phononic plates, structured with metallic arrays on their surfaces and loaded with inductive circuits. These structures, studied experimentally and theoretically, exhibit a variety of localized and/or extended in frequency modes that originate from an electric circuit behavior related to the inductive loads and span the low, intermediate, or high frequency range in a typical dispersion plot. This low-pass, band-pass, and high-pass behavior that manifests itself as an important potential variation along these trajectories, combined to the automatized, controllable character of our experimental device, constitute a powerful tool for applications targeting real-time manipulation of elastic waves via EM waves and vice-versa. We demonstrate the appearance of unusual, high-valued, positive or negative group-velocity branches, not encountered in typical Lamb-like dispersion plots of phononic plates, easily tuned via the external inductive loads.

Our experimental results, enhanced by non-ordinary, high-resolution signal processing techniques, are in accordance with the theoretical predictions —despite some isolated discrepancies; they confirm the basic underlying mechanisms analyzed in this paper and the main phenomonogical aspects that interest us for applications, our aim being among others the realization of viable, simple devices that can operate under real conditions and produce the desired effects in the modulation of the dispersion properties of these crystals. Nevertheless, although its very application-oriented aspect at a first sight, this study councils *per se* an important physical insight.

DATA AVAILABILITY STATEMENT

The data that support the findings of this study are available from the corresponding author upon reasonable request.

Appendix A: Equivalent electric circuits

A piezoceramic plate with metallized surfaces can be effectively described by an equivalent capacitor. When metallic strips are structured periodically on its both surfaces, we can use an equivalent picture of a periodic transmission line whose unit cell coincides with the unit cell of the real structure. We give in what follows the electric-circuit models that correspond to such a description for the cases studied in this paper.

1. Two-atom grounded-L crystal

The equivalent circuit that models the two electric resonators shown in Fig. 3(a) when the piezoelectric coupling is switched off is depicted in Fig. 10(a). We define all voltages in the input, V_{A_j}, and output, $V_{B_j} = \mathcal{P}V_{A_j}$, of the unit cell with respect to a common ground reference, where $j = 1, 2$, and $\mathcal{P} = \mathrm{e}^{-\mathrm{i}k_1 a}$ is the Bloch phase factor (we assume an $\mathrm{e}^{+\mathrm{i}\omega t}$ time dependance in all fields);

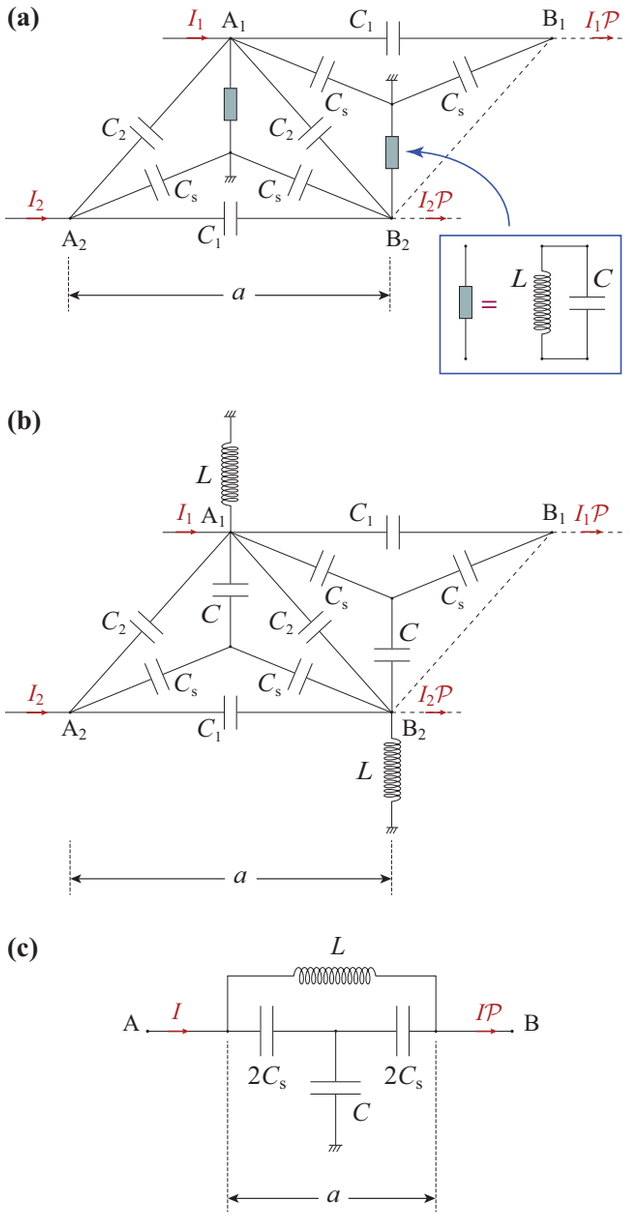

FIG. 10. The unit cell of a periodic transmission line describing equivalently (a) the two-atom grounded-L crystal [Fig. 3(a)], (b) the two-atom floating-potential-L crystal [Fig. 3(b)], and (c) the intercellular-L crystal [Fig. 3(c)], when electromechanical coupling is switched off.

the incoming and outgoing electric currents are respectively I_j and $\mathcal{P}I_j$. Application of Kirchhoff's current and voltage laws leads to a secular equation depending only on $\mathcal{P}$ and the set of unit-cell impedances. We thus obtain the following dispersion equation for the two electric resonant bands

$$\omega^{\pm}(k_1) = \left[LC\left(1+2\frac{C_s+C_1+C_2}{C}\right.\right. \qquad \text{(A1)}$$
$$\left.\left. - 2\frac{C_1}{C}\cos k_1 a \mp 2\frac{C_2}{C}\cos\frac{k_1 a}{2}\right)\right]^{-1/2}.$$

At Γ point (center of the BZ) the two distinct eigenfrequencies are $\omega_0^+ = \left[LC\left(1+2\frac{C_s}{C}\right)\right]^{-1/2}$ and $\omega_0^- = \left[LC\left(1+2\frac{C_s+2C_2}{C}\right)\right]^{-1/2}$, corresponding to a *bonding* and an *antibonding* mode; at X point (edges of the BZ) a double degenerate eigenfrequency is found to be $\omega_\pi = \left[LC\left(1+2\frac{C_s+2C_1+C_2}{C}\right)\right]^{-1/2}$. The width $\Delta\omega^{\pm} = |\omega_0^{\pm} - \omega_\pi|$ of these cos-like resonant bands is finite, and controlled by L and the internal effective parameters of the model C, C_s, C_1 and C_2. We note that these capacitors do not correspond to real electronic elements in our device, but they describe its equivalent behavior. C and C_s account for a capacitive effect between electrodes located at the two opposite sides (i.e., along x_3-direction) and at the same side (i.e., along x_1-direction) of the plate, respectively. C_1 and C_2 describe the capacitive interaction between electrodes of the same side at distance $a = 2a_0$ and between electrodes at the opposite sides at distance $R = \sqrt{a_0^2+h^2}$, respectively, in one-to-one analogy with the overlapping coefficients γ_1, γ_2 of the tight-binding model.

2. Two-atom floating-potential-L crystal

For the case of the two-atom crystal with an alternation of floating-potential EBCs and inductance loads — its unit cell is given in Fig. 3(b)— we proceed in a similar manner to construct its equivalent circuit [see Fig. 10(b)] that models the two electric resonators. Using the same steps as for the previous case, we obtain, after a relatively lengthy but straightforward algebra, the following dispersion equation for the two electric bands

$$\omega^{\pm}(k_1) = \left\{2LC\left[\frac{C_1+2C_2}{C} + \frac{C_s}{C}\frac{2C+C_s}{C+2C_s}\right.\right. \qquad \text{(A2)}$$
$$- \left(\frac{C_1}{C} + \frac{C_s}{C}\frac{C_s}{C+2C_s}\right)\cos k_1 a$$
$$\left.\left. \mp\, 2\left(\frac{C_2}{C} + \frac{C_s}{C+2C_s}\right)\cos\frac{k_1 a}{2}\right]\right\}^{-1/2}.$$

At Γ point two distinct eigensolutions are found, one finite $\omega_0^- = \left[8LC_2\left(1+\frac{C}{C_2}\frac{C_s}{2C_s+C}\right)\right]^{-1/2}$ and one diverging as $\omega_0^+ \sim \left[LC_1\left(1+\frac{C_s}{C_1}\frac{C_s}{2C_s+C}\right)\right]^{-1/2}(k_1 a)^{-1}$. The higher frequency branch $\omega^+(k_1)$ behaves as an hyperbolic function for $k_1 a \ll 1$, while the lower frequency branch $\omega^-(k_1)$ corresponds to a cos-like resonant band of finite width $\Delta\omega^- = |\omega_0^- - \omega_\pi|$, where ω_π is the common, double degenerate eigenfrequency at X point, found to be $\omega_\pi = \left[4L\left(C_1+C_2+C_s\frac{C+C_s}{C+2C_s}\right)\right]^{-1/2}$. The form of these two dispersive modes is still controlled by L and the internal effective parameters of the model C, C_s, C_1

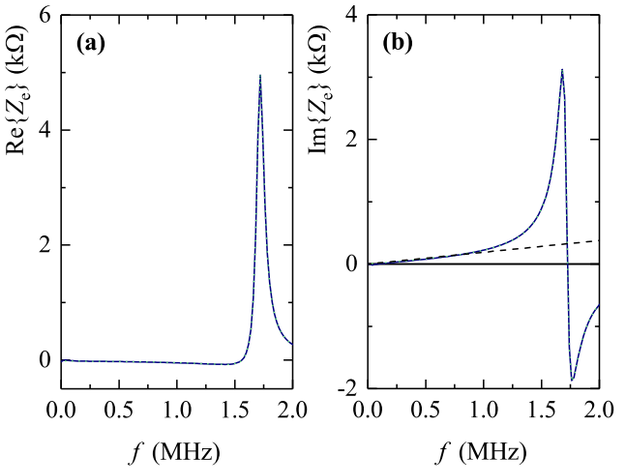

FIG. 11. Real (a) and imaginary (b) part of the impedance load Z_e used in the external circuits of Fig. 3. Solid and dotted lines represent the real (measured) and modeled [Eq. (B1)] function, respectively; in (b) the impedance of a pure inductance $L = 30$ μH is also shown (broken line) for comparison.

and C_2, whose physical meaning is the same as that for the grounded-L crysral.

3. Intercellular-L crystal

The unit cell of Fig. 3(c) is modeled by the periodic transmission line whose unit cell is shown in Fig. 10(c). We easily obtain the following dispersion relation

$$\omega(k_1) = \omega_0 \left[\frac{C}{4C_s} + \left(2 \sin \frac{k_1 a}{2} \right)^{-2} \right]^{-1/2},$$
$$\omega_0 = \left[\frac{1}{LC} \left(1 + \frac{C}{4C_s} \right) \right]^{1/2} \tag{A3}$$

from which one can immediately deduce the angular frequency at X point, $\omega_\pi = \frac{1}{\sqrt{LC_s}}$, and the effective medium velocity at the long wavelength limit $c_{\text{eff}} = \lim_{k_1 \to 0} \frac{\omega}{k_1} = a\omega_0$. In this simplified but still quite accurate model, knowledge of two external parameters, e.g. ω_π and ω_0 (or, equivalently, c_{eff}), is sufficient to determine the internal model parameters, C and C_s.

Appendix B: Impedance-load function

The external impedance load is ideally assumed to be an inductance L connected to the metallic strips, as detailed in Fig. 3. However, in practice, the real component, used in our experiments, has not a pure inductive behavior; other contributions have to be taken into account, related to several internal circuitry parts of resistive and/or capacitive type of this component. The measured impedance Z_e of our individual component —a representative one, extracted from the crystal— is plotted in Fig. 11 against frequency, f, and both its real and imaginary parts [plots (a) and (b), respectively] show a resonant behavior at about 1.71 MHz. Within the frequency range that interest us here (up to 2 MHz) this function can be in a very good approximation described by the following rational expression

$$Z_e = \frac{\alpha_4 f^4 + \alpha_3 f^3 + \alpha_2 f^2 + \alpha_1 f + \alpha_0}{f^2 + \beta_1 f + \beta_0} \tag{B1}$$
$$= \gamma_0 + \gamma_1 f + \gamma_2 f^2 + \frac{\delta_+}{f - f_+} + \frac{\delta_-}{f - f_-}$$

where f is expressed in MHz in the above expressions, and α_n and β_n are appropriate complex coefficients obtained by a fitting procedure

$$\begin{aligned}
\alpha_4 &= -5.15566 - \mathrm{i}\, 5.18013 \times 10^{-14}, \\
\alpha_3 &= -6.96706 \times 10^{-14} + \mathrm{i}\, 22.0970, \\
\alpha_2 &= 52.4644 + \mathrm{i}\, 4.78721 \times 10^{-13}, \\
\alpha_1 &= 4.56112 \times 10^{-13} - \mathrm{i}\, 452.779, \\
\alpha_0 &= 56.4767 - \mathrm{i}\, 7.41831 \times 10^{-13}, \\
\beta_1 &= -7.61040 \times 10^{-17} - \mathrm{i}\, 0.0790166, \\
\beta_0 &= -2.94215 + \mathrm{i}\, 8.96296 \times 10^{-18},
\end{aligned} \tag{B2}$$

and

$$\begin{aligned}
\gamma_0 &= \alpha_2 - \alpha_3\beta_1 + \alpha_4(\beta_1^2 - \beta_0) \\
&= 35.5818 + \mathrm{i}\, 3.22798 \times 10^{-13}, \\
\gamma_1 &= \alpha_3 - \alpha_4\beta_1 \\
&= -6.59699 \times 10^{-14} + \mathrm{i}\, 21.6896, \\
\gamma_2 &= \alpha_4, \\
\delta_\pm &= \pm 51.4400 - \mathrm{i}\, 193.077, \\
f_\pm &= \frac{1}{2}\left(-\beta_1 \pm \sqrt{\beta_1^2 - 4\beta_0} \right) \\
&= \pm 1.71481 + \mathrm{i}\, 0.0395083.
\end{aligned} \tag{B3}$$

[1] M. Leamy, M. Carrara, A. Erturk, M. Cacan, and M. Ruzzene, "Metamaterial-inspired structures and concepts for elastoacoustic wave energy harvesting," *Smart Mater. Struct.* **22**, 065004 (2013).
[2] J. Li, X. Zhou, G. Huang, and G. Hu, "Acoustic metamaterials capable of both sound insulation and energy harvesting," *Smart Mater. Struct.* **25**, 045013 (2016).
[3] L. Wu, Y. Wang, K. Chuang, F. Wu, Q. Wang, W. Lin, and H. Jiang, "A brief review of dynamic mechanical metamaterials for mechanical energy manipulation," *Mater. Today* **44**, 168–193 (2021).
[4] Z. Liu, X. Zhang, Y. Mao, Y.Y. Zhu, Z. Yang, C.T. Chan, and P. Sheng, "Locally resonant sonic materials," *Science* **289**, 1734–1736 (2000).
[5] J. Li and C.T. Chan, "Double-negative acoustic metamaterial," *Phys. Rev. E* **70**, 055602(R) (2004).
[6] A. Ba, A. Kovalenko, C. Aristégui, O. Mondain-Monval, and T. Brunet, "Soft porous silicone rubbers with ultra-low sound speeds in acoustic metamaterials," *Sci. Rep.* **7**, 40106 (2017).
[7] P. Celli, B. Yousefzadeh, C. Daraio, and S. Gonella, "Bandgap widening by disorder in rainbow metamaterials," *Appl. Phys. Lett.* **114**, 091903 (2019).

[8]M. Miniaci, A. Krushynska, A.S. Gliozzi, N. Kherraz, F. Bosia, and N.M. Pugno, "Design and Fabrication of Bioinspired Hierarchical Dissipative Elastic Metamaterials," *Phys. Rev. Applied* **10**, 024012 (2018).

[9]Q.J. Lim, P. Wang, S.J.A. Koh, E.H. Khoo, and K. Bertoldi, "Wave propagation in fractal-inspired self-similar beam lattices," *Appl. Phys. Lett.* **107**, 221911 (2015).

[10]J.-F. Robillard, O. Bou Matar, J.O. Vasseur, P.A. Deymier, M. Stippinger, A.-C. Hladky-Hennion, Y. Pennec, and B. Djafari-Rouhani, "Tunable magnetoelastic phononic crystals," *Appl. Phys. Lett.* **95**, 124104 (2009).

[11]W. Qian, Z. Yu, X. Wang, Y. Lai, and B.B. Yellen, "Elastic metamaterial beam with remotely tunable stiffness," *J. Appl. Phys.* **119**, 055102 (2016).

[12]S.W. Xiao, G.C. Ma, Y. Li, Z.Y. Yang, and P. Sheng, "Active control of membrane-type acoustic metamaterial by electric field," *Appl. Phys. Lett.* **106**, 91904 (2015).

[13]Y. Cheng, X.J. Liu, and D.J. Wu, "Temperature effects on the band gaps of lamb waves in a one-dimensional phononic-crystal plate," *J. Acoust. Soc. Am.* **129**, 1157–1160 (2011).

[14]Z. Li, Y. Li, S. Kumar, and H.P. Lee, "Thermal tuning of negative effective mass density in a two-dimensional acoustic metamaterial with hexagonal lattice," *J. Appl. Phys.* **126**, 155102 (2019).

[15]E. Walker, D. Reyes, M.M. Rojas, A. Krokhin, Z. Wang, and A. Neogi, "Tunable ultrasonic phononic crystal controlled by infrared radiation," *Appl. Phys. Lett.* **105**, 143503 (2014).

[16]A.S. Gliozzi, M. Miniaci, A. Chiappone, A. Bergamini, B. Morin, E. Descrovi, "Tunable photo-responsive elastic metamaterials," *Nat. Comm.* **11**, 2576 (2020).

[17]L. Airoldi and M. Ruzzene, "Design of tunable acoustic metamaterials through periodic arrays of resonant shunted piezos," *New J. Phys.* **13**, 113010 (2011).

[18]R. Zhu, Y.Y. Chen, M.V. Barnhart, G.K. Hu, C.T. Sun, and G.L. Huang, "Experimental study of an adaptive elastic metamaterial controlled by electric circuits," *Appl. Phys. Lett.* **108**, 011905 (2016).

[19]C. Sugino, M. Ruzzene, and A. Erturk, "Design and analysis of piezoelectric metamaterial beams with synthetic impedance shunt circuits," *IEEE/ASME Trans. Mechatronics* **23**, 2144–55 (2018).

[20]S. Degraeve, C. Granger, B. Dubus, J.O. Vasseur, M. Pham Thi, and A.-C. Hladky-Hennion, "Bragg band gaps tunability in an homogeneous piezoelectric rod with periodic electrical boundary conditions," *J. Appl. Phys.* **115**, 194508 (2014).

[21]S. Degraeve, C. Granger, B. Dubus, J.O. Vasseur, M. Pham Thi, and A.-C. Hladky-Hennion, "Tunability of Bragg band gaps in one-dimensional piezoelectric phononic crystals using external capacitances," *Smart Mater. Struct.* **24**, 085013 (2015).

[22]S.A. Mansoura, P. Benard, B. Morvan, P. Marechal, A.-C. Hladky-Hennion, and B. Dubus, "Theoretical and experimental analysis of a piezoelectric plate connected to a negative capacitance at MHz frequencies," *Smart Mater. Struct.* **24**, 115032 (2015).

[23]N. Kherraz, L. Haumesser, F. Levassort, P. Benard, and B. Morvan, "Controlling Bragg gaps induced by electric boundary conditions in phononic piezoelectric plates," *Appl. Phys. Lett.* **108**, 093503 (2016).

[24]N. Kherraz, L. Haumesser, F. Levassort, P. Benard, and B. Morvan, "Hybridization bandgap induced by an electrical resonance in piezoelectric metamaterial plates," *J. Appl. Phys.* **123**, 094901 (2018).

[25]N. Kherraz, F.H. Chikh-Bled, R. Sainidou, B. Morvan, and P. Rembert, "Tunable phononic structures using Lamb waves in a piezoceramic plate," *Phys. Rev. B* **99**, 094302 (2019).

[26]F.H. Chikh-Bled, N. Kherraz, R. Sainidou, P. Rembert, and B. Morvan, "Piezoelectric phononic plates: retrieving the frequency band structure via all-electric experiments," *Smart Mater. Struct.* **28**, 115046 (2019).

[27]We used the COMSOL Multiphysics v. 5.5 software to perform the calculations (www.comsol.com. COMSOL AB, Stockholm, Sweden).

[28]https://www.americanpiezo.com/.

[29]M. Tummala, "New algorithm for solving block matrix equations with applications in 2-D AR spectral estimation," *IEEE Trans. Signal Processing* **39**, 759–764 (1991).

[30]N. W. Ashcroft and N. D. Mermin, *Solid State Physics* (New York: Saunders College Publishing, 1976).

[31]The equivalent electric circuit that models this unit cell coincides to that shown in Fig.A1(b) of Ref. 26, and the dispersion relation of this mode is still given by Eq.(2) of the above-mentionned reference.

[32]R. Sainidou, N. Stefanou, I.E. Psarobas, and A. Modinos, "Scattering of elastic waves by a periodic monolayer of spheres," *Phys. Rev. B* **66**, 024303 (2002).

AIP Publishing
Journal of Applied Physics
ACCEPTED MANUSCRIPT

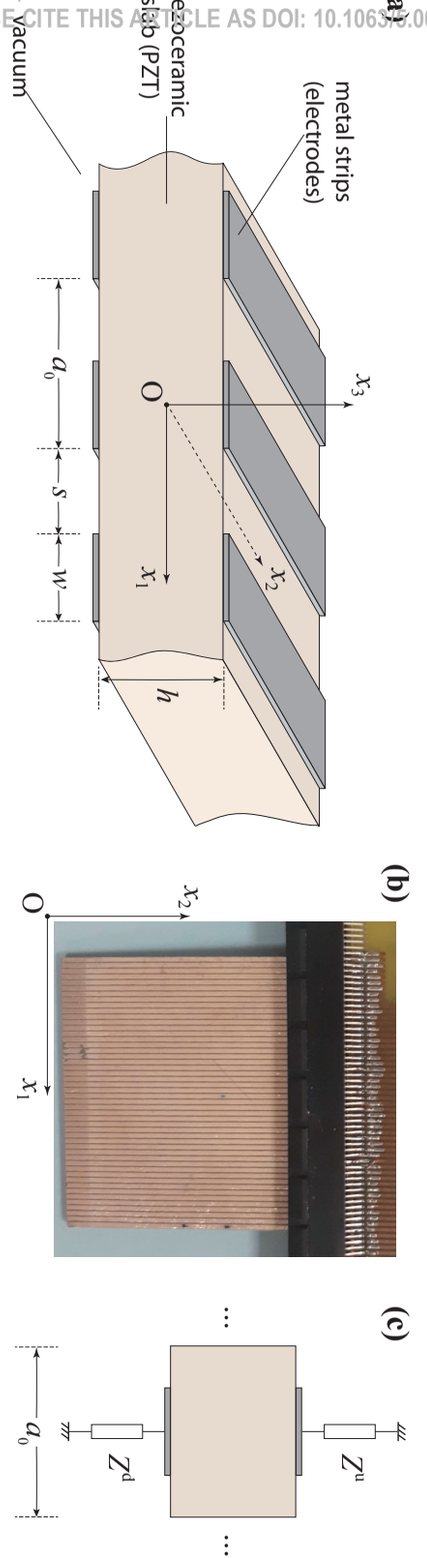

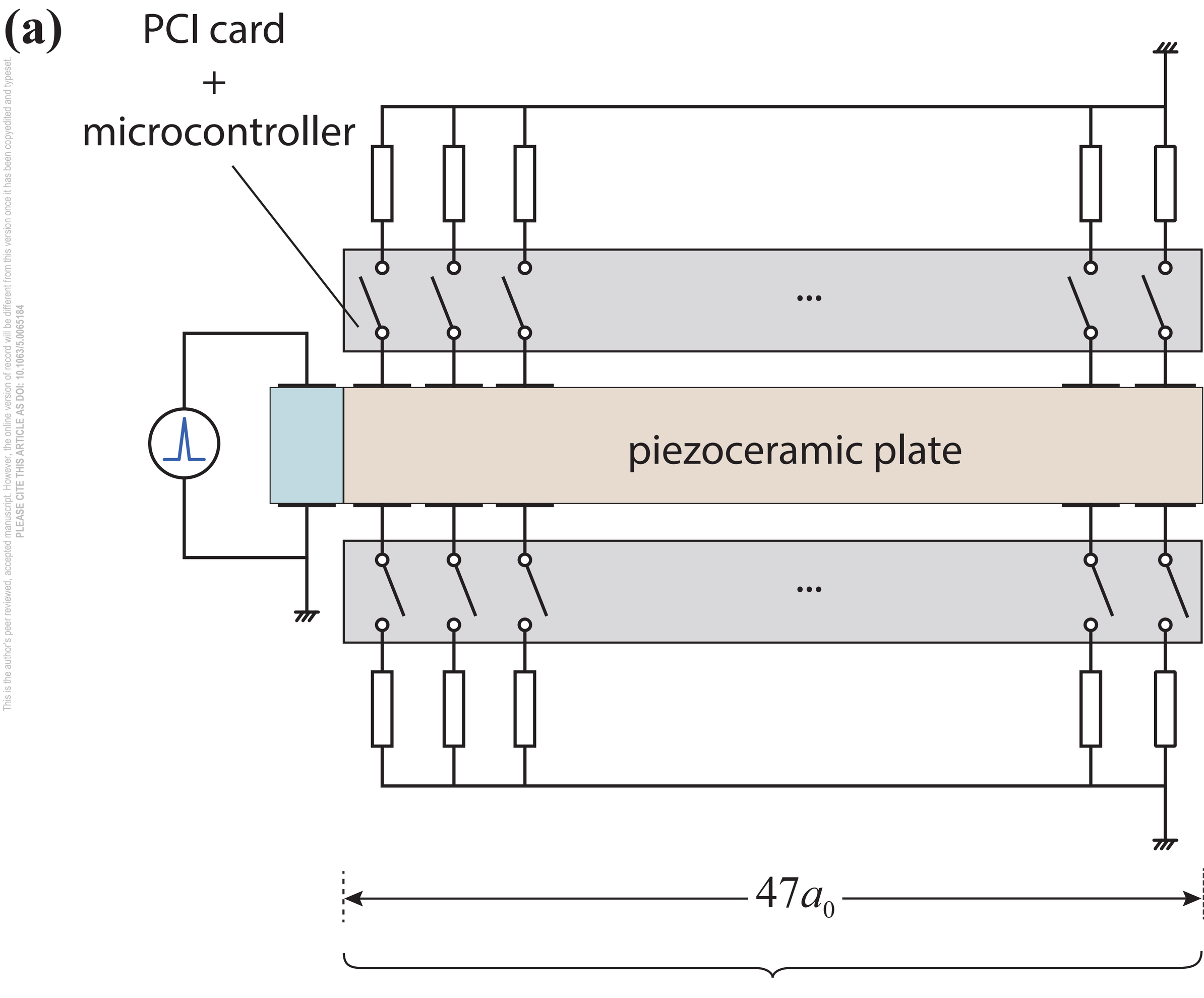

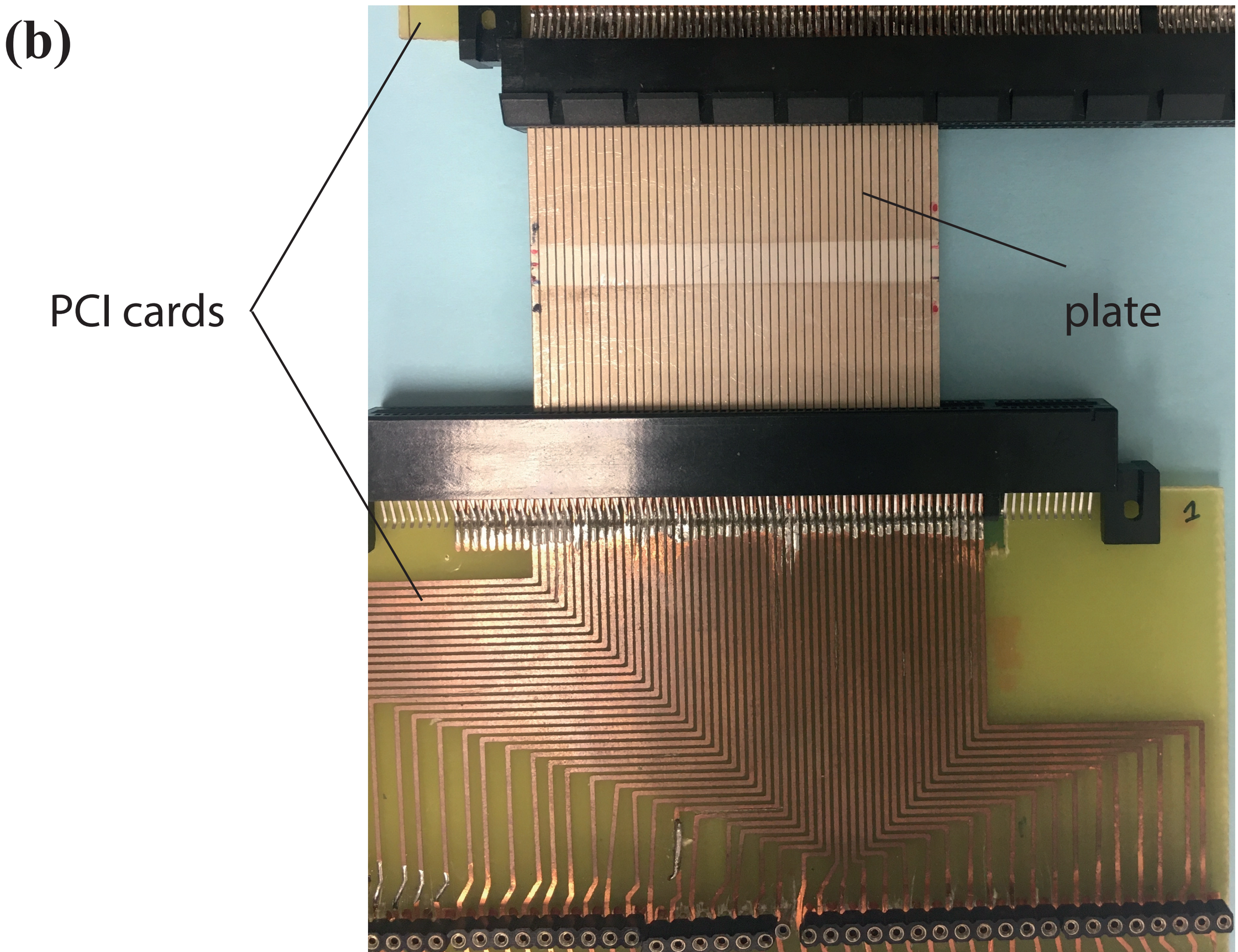

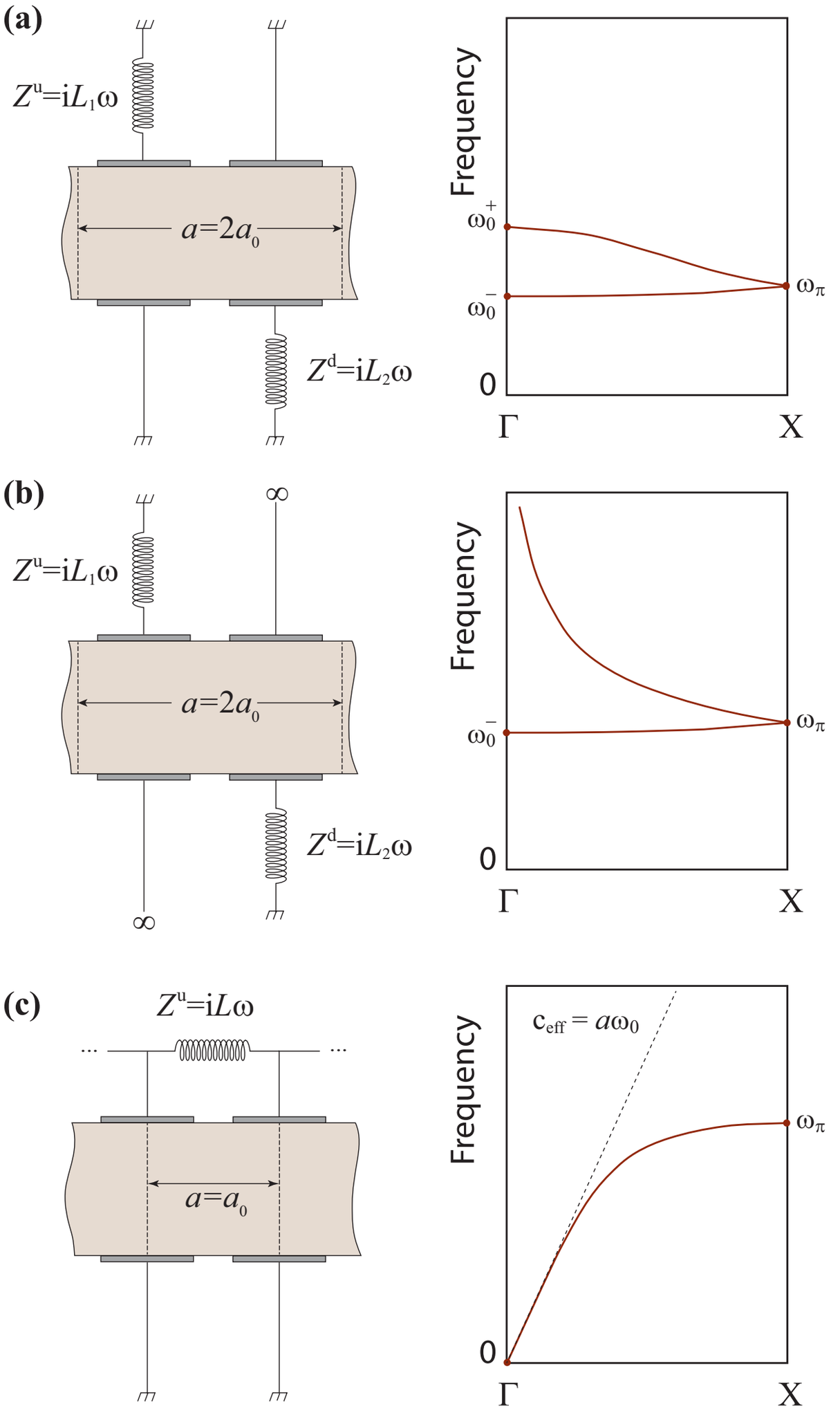

Journal of Applied Physics

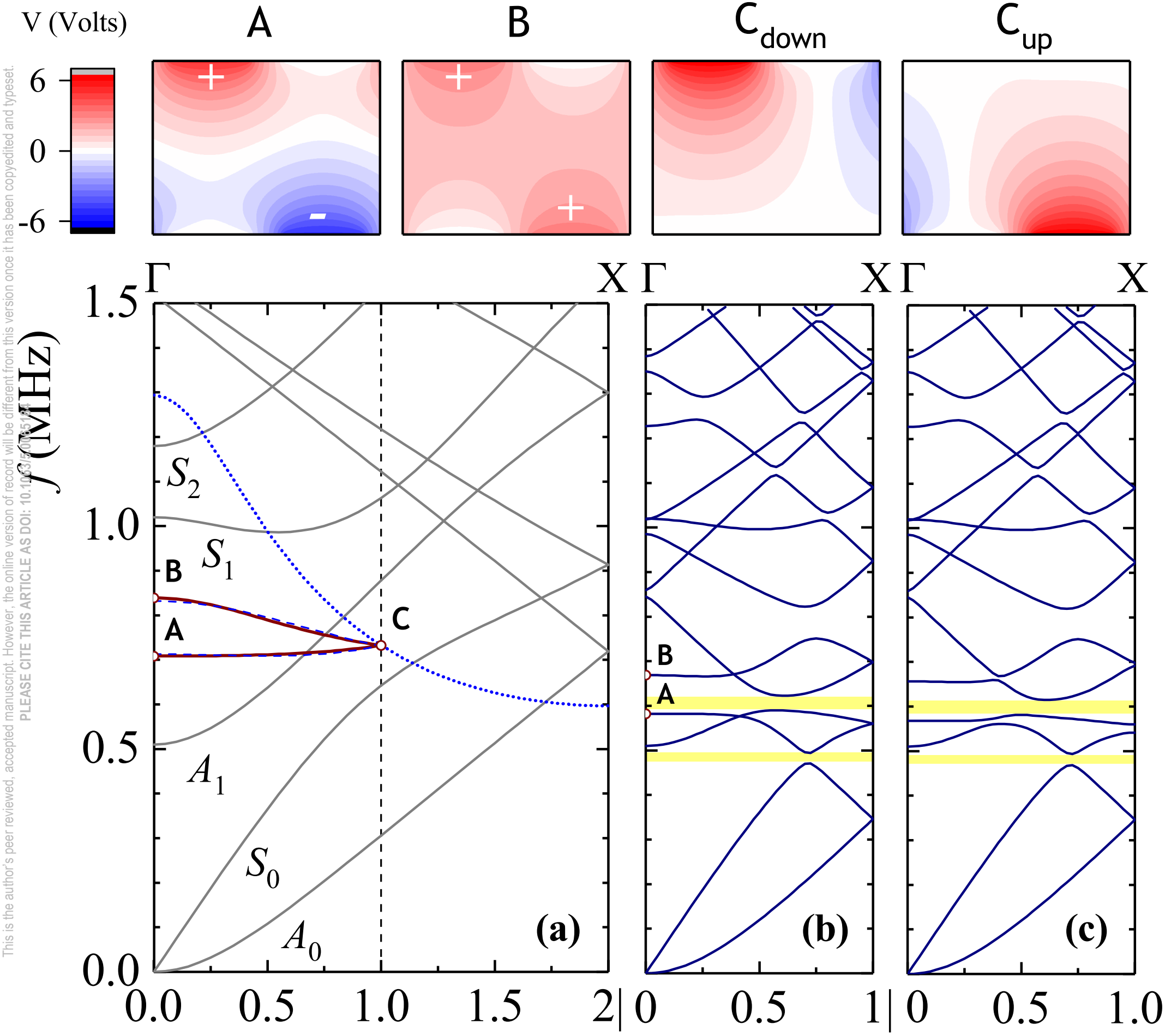

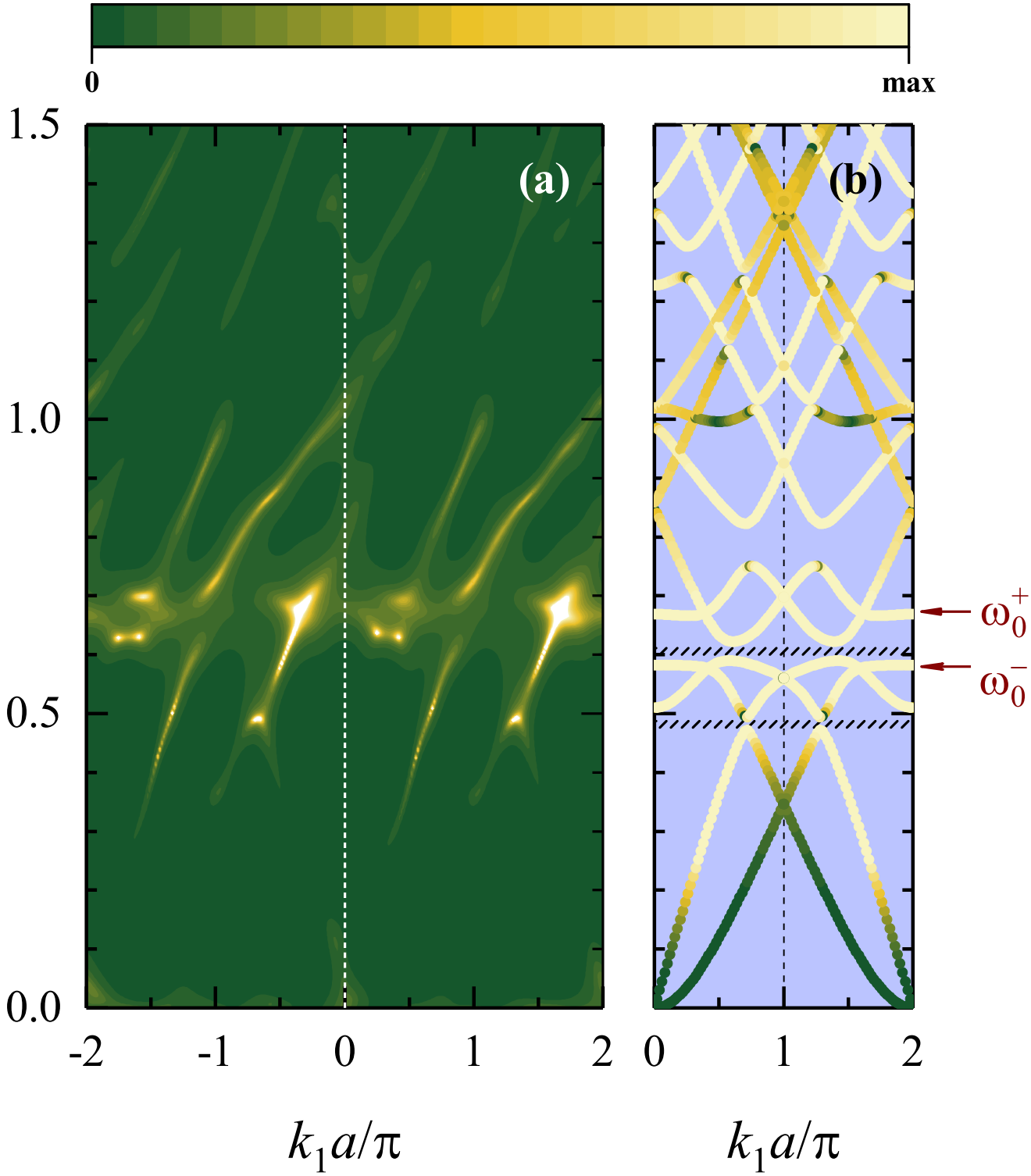

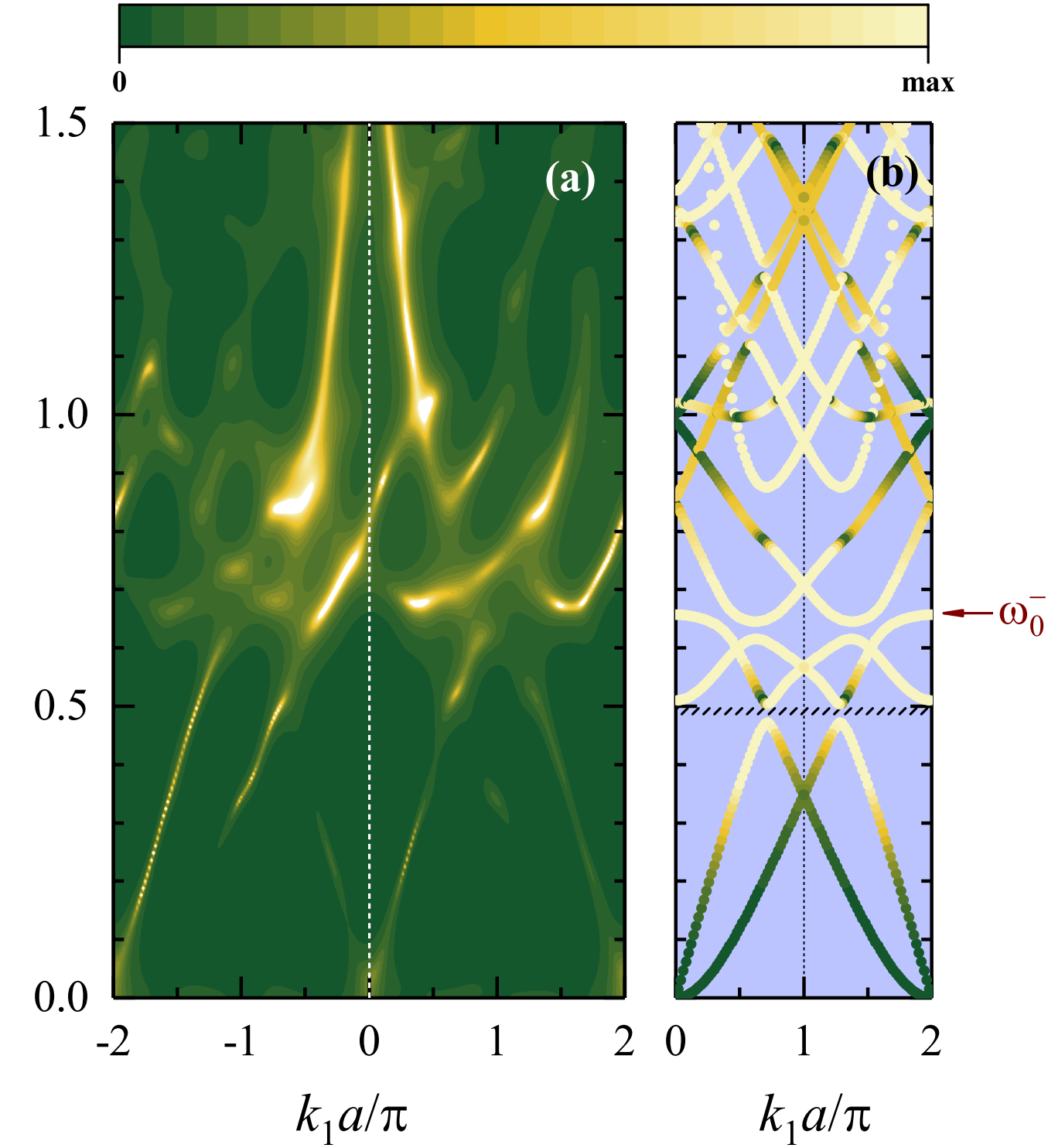

AIP Publishing

Journal of Applied Physics

ACCEPTED MANUSCRIPT

This is the author's peer reviewed, accepted manuscript. However, the online version of record will be different from this version once it has been copyedited and typeset.
PLEASE CITE THIS ARTICLE AS DOI: 10.1063/5.0065184